Catalytic pyrolysis of crude glycerol over shaped ZSM-5/bentonite catalysts for bio-BTX synthesis

Songbo He[a], I. Muizebelt[b], A. Heeres[b,c], N.J. Schenk[b], R. Blees[b], H.J. Heeres[a,*]

[a] Green Chemical Reaction Engineering, Engineering and Technology Institute Groningen, University of Groningen, Nijenborgh 4, 9747 AG Groningen, The Netherlands
[b] Bio-BTX BV, De Mudden 14, 9747 AW Groningen, The Netherlands
[c] Hanze University of Applied Sciences, Zernikeplein 11, 9747 AS Groningen The Netherlands

ARTICLE INFO

ABSTRACT

Ex-situ catalytic pyrolysis of crude glycerol for the synthesis of bio-based benzene, toluene and xylenes (bio-BTX) was performed in a tandem micro-reactor (TMR), a batch gram scale reactor and a continuous integrated bench scale unit using ZSM-5/bentonite extrudates. A bio-BTX yield of 8.1 wt.% (14.6% carbon yield) based on crude glycerol was obtained over the fresh catalysts (Cat-F) in the bench scale unit (crude glycerol feed rate of 200 g h^{-1}, pyrolysis temperature of 520 °C and catalytic upgrading temperature of 536 °C). Catalyst activity was shown to be a function of the time on stream (TOS) and after 4.7 h the activity dropped with about 8%. After an oxidative regeneration step to remove coke, the activity of the regenerated catalysts (Cat-R1) was recovered to 95% of the original catalyst activity. After 11 reaction-regeneration cycles, the bio-BTX yield decreased to 5.4 wt. % (9.7% carbon yield) over Cat-R11. The fresh, deactivated and regenerated ZSM-5/bentonite catalysts were characterized in detail using nitrogen physisorption, XRD, ICP-AES, EA, TEM-EDX, TGA, NH$_3$-TPD, pyridine-IR and solid MAS NMR. Coke (10.5 wt.% over Cat-D) was mostly deposited on ZSM-5 planes, and not only decreased the number of Lewis and Brönsted acid sites, but also blocked the pores, resulting in catalyst deactivation. Coke removal was effectively performed using an oxidative treatment. However, exchange of cations (e.g., Na) of the bentonite and possibly also from the crude glycerol feed with protons of ZSM-5 was observed, leading to irreversible deactivation. Furthermore, the layered structure of bentonite collapsed due to the removal of interlamellar water and dehydroxylation.

1. Introduction

The biodiesel industry has grown substantially in the last two decades [1]. However, its production inevitably leads to the formation of glycerol (ca. 10% (wt./wt.)). The worldwide crude glycerol production is expected to grow further to 6 million ton in 2025 [2]. The identification of high value applications of glycerol would significantly improve the profitability and sustainablity of the biodiesel industry.

Glycerol has been recognized as an interesting 'green building' block for the chemical industry. Various examples [3,4] have been reported for the conversion of glycerol by oxidation, hydrogenolysis, dehydration, esterification/etherification, pyrolysis/gasification and steam reforming, etc. In addition, glycerol pyrolysis has also been studied in detail. Thermogravimetric analysis (TGA) revealed that pyrolysis products are generated at temperatures between 150 and 500 °C [5]. Thermal (non-catalytic) pyrolysis of glycerol mainly leads to the formation of non-condensable gases (e.g., H$_2$, CO, CH$_4$ and C$_2$H$_4$) when performed at relatively long residence times (e.g., 22 s) [6] and

condensable gases (e.g., acrolein and acetaldehyde) using very short residence times (e.g., 0.1 s) [7].

An interesting option is the conversion of glycerol using catalytic pyrolysis to produce bio-based low molecular weight aromatics (benzene, toluene and xylenes, termed as bio-BTX), which are intermediates for the synthesis of a wide range of polymers. This may be achieved by using both in situ and ex-situ approaches. In the latter case, proper catalysts are used to upgrade the glycerol pyrolysis vapors. It has been shown that glycerol is first dehydrated into oxygenates (mainly acrolein and acetaldehyde), followed by a series of acid-catalyzed aldol condensation, dissociation, cyclization and oligomerization, etc., to form aromatics [6–10]. Hoang et al. [11] were the first to report on the catalytic pyrolysis of glycerol over a series of zeolites in a fixed bed reactor. It was shown that aromatics are favorably formed on zeolites with three-dimensional medium sized pores (e.g., ZSM-5, BTX carbon yield of 7.4%). Lowering the SiO$_2$/Al$_2$O$_3$ mole ratio, leading to higher Brönsted acidity, favored aromatization [9] resulting in a higher BTX yield [9,12]. However, simultaneously, the hydrophilicity is also

increased which inhibits acid-catalysed dehydration reactions [9]. A maximum BTX yield was obtained using ZSM-5 with a SiO_2/Al_2O_3 mole ratio of 30 [9,12]. The co-feeding of H_2, which is referred as catalytic hydro-pyrolysis, has a positive effect on BTX yields. For instance, carbon yields of 18.1% over a tandem Pt/ZnO and ZSM-5 catalyst [11] and carbon yields of 42.9% over bi-functional Pd/ZSM-5 catalysts have been reported [13].

Besides the use of hydrogen, higher BTX yields can also be obtained by introduction of metals in the framework of the ZSM-5 zeolite. For instance, the introduction of Zn ions by Zn-proton exchange enhanced the BTX yield considerably [10,12,14] by suppressing hydrogen transfer reactions favoring olefin formation and providing dehydrogenation sites for dehydrocyclization [9]. Similarly, higher BTX yields were also observed by the introduction of Ga [12], Mo [10,12], Cu [12], Ni [10], Ag [10] and Sn [10] in the zeolite framework. Furthermore, Xiao *et al.* [15] observed that NaOH treated ZSM-5 gives higher yields of BTX due to the generation of mesopores as well as the formation of a zeolite with an optimum ratio between Brönsted and Lewis acid sites. Besides ZSM-5 based catalysts, the use of Al_2O_3 [16] and Pd and Ru catalysts thereof [17] were also explored, though relatively low BTX yields (2 wt.%) were obtained [16].

Dilution of the glycerol, *e.g.,* with water, has also shown to lead to higher BTX yields [12]. For instance, Zhang *et al.* [11] obtained a BTX carbon yield of 16.5% for the catalytic pyrolysis of 12.5 wt.% glycerol/water over ZSM-5 catalysts. Co-feeding with lower alcohols (*e.g.*, CH_3OH [10,12,14,16,18–20] and CH_3CH_2OH [12,16]), low molecular weight aromatics (*e.g.*, benzene and toluene [19]) and alkanes (*e.g.*, hexane [17], dodecane and hexadecane [16]) have been intensively studied to obtain higher BTX yields, to tune the individual amounts of benzene, toluene and xylenes in the BTX mixture and to extend catalyst life-time.

Most investigations on the catalytic pyrolysis of glycerol focussed on the use of powdered catalysts or pressed pellets with small particle size (max. 40–60 mesh). However, when using *ex-situ* approaches with vapour phase upgrading using a packed at larger scale, these are not suitable and shaped catalysts with larger particle sizes are needed. Such larger catalysts (*e.g.*, extrudes and spheres) are typically made using a binder (*e.g.*, bentonite [14]). It has been reported that the addition of bentonite hardly affects the BTX yields, even at high bentonite amounts (82%) [14]. However, investigations on the use of larger mm sized ZSM-5/bentonite particles for the catalytic pyrolysis of glycerol with respect to catalyst performance (BTX yield), catalyst life-time (time on stream), catalyst deactivation, catalyst regenerability and reusability have not been reported to date.

In this manucript, we demonstrate the *ex-situ* catalytic pyrolysis of crude glycerol for bio-BTX synthesis in a continuous dedicated bench scale unit containing 200 g catalyst with dimension of relevance for industrial operation in packed bed reactors. For this purpose, we made ZSM-5/bentonite extrudates with particle size between 1–2 mm, and examined the catalyst performance with respect to BTX yield, carbon yield, mass and carbon balance closure. The activity and stability of the ZSM-5/bentonite catalysts was systemically investigated for 11 reaction/regeneration cycles to examine the regenerability and reusability. The deactivated and regenerated catalysts were analyzed in detail (BET, XRD, ICP-AES, EA, TEM-EDX, TGA, NH_3-TPD, pyridine-IR and solid MAS NMR) to obtain insight in both reversible and irreversible catalyst deactivation phenomena.

2. Experimental

2.1. Materials

ZSM-5(23) powder (Product number CBV2314) in the ammonium form was supplied by Zeolyst International (USA). Bentonite powder (Product number 285234, CAS number 1302-78-9) was obtained from Sigma-Aldrich Corporation (USA). Crude glycerol, which is a mixture of

Table 1
Composition of the crude glycerol used in this study.

H_2O^a (wt.%)	CH_3OH^b (wt.%)	Glycerol^c (wt.%)	FAME^c (wt.%)	FFA^c (wt.%)	Na^d (wt.%)	Mg^d (wt.%)	Fe^d (wt.%)
2.43	0.05	49	4.3	44.5	0.76	< 0.01	0.03

FAME: fatty acid methyl ester.
FFA: free fatty acids.
  [a] Karl Fisher analysis.
  [b] trace GC analysis.
  [c] ^1H NMR.
  [d] AAS.

glycerol and fatty acids (Table 1), was commercially supplied by Sunoil Biodiesel B.V., The Netherlands.

2.2. Catalyst preparation

The as-received ZSM-5(23) and bentonite powders were pre-calcined separately at 550 °C for 8 h. For the ZSM-5(23) powder, this converts the ammonia form to the H-ZSM-5 form (termed as ZSM-5). The two calcined powders were then mixed with different weight ratios (90:10, 80:20 and 60:40, ZSM-5:bentonite) in a Multilab Mixer/Extruder/Spheronizer (Caleva, UK) followed by adding distilled water (0.45 g per gram powder) to produce wet extrudes with an outer diameter (OD) of 1 mm and length of 1 mm. The extrudes were dried at 110 °C for 12 h, followed by calcination in a LT 9/11/P330 Muffle Furnace (Nabertherm, Germany) at 550 °C for 5 h at a heating rate of 5 °C min^{-1}. The final catalysts with particle sizes of 1–2 mm were obtained after a calcination for 8 h.

2.3. Catalytic pyrolysis of glycerol

2.3.1. Catalyst screening in a batch micro-reactor (with glycerol loading of 1 mg)

A Rx-3050TR Tandem micro-Reactor (TMR, Frontier Lab, Japan) was employed to rapidly screen the effect of the ZSM-5 to bentonite ratio on catalyst performance. Pure glycerol (1 mg) was charged to the pyrolysis reactor, catalysts (70 mg, 212–425 μm) were charged to the fixed bed reactor. The catalysts were preheated at 550 °C for 30 min under a He flow (54 ml min^{-1}) and maintained at 550 °C during reaction. The pyrolysis of glycerol was performed at 500 °C. The products were analyzed using an on-line HP5890/HP5972 GC–MS (Agilent, USA) equipped with Rx1-5Sil column (30m × 0.25 mm × 10 μm, Restek, USA). The BTX yield was calculated using a single point external calibration.

2.3.2. Experiments in a batch gram scale reactor

A tandem fixed bed reactor heated in a fluidized sand bath (T_{set} = 550 °C) was used to determine the mass and carbon balances during the *ex-situ* catalytic pyrolysis of crude glycerol. The upper bed is used for the thermal pyrolysis of crude glycerol (1 g) under a flow of N_2 gas (11 mL/min), whereas the lower one is for the catalytic aromatization of the pyrolysis vapor over 3 g catalysts. The reactor configuration was designed in such a way to enable stepwise submersion of both beds in the fluidized sand bath. The lower catalyst bed was first submerged to preheat the catalyst until the temperature of the upper bed reached 85 °C. Then, the upper bed was submerged into the sand bath and was kept for 15 min to fulfill the *ex-situ* catalytic pyrolysis of crude glycerol. All the products were transferred to a stainless vessel, which was immersed into a cold trap at −40 to −50 °C, to condense, separate and collect the liquid products. The non-condensable gaseous products were all collected in a gas bag. When the *ex-situ* catalytic pyrolysis was finished, the whole reactor was lifted from the sand bath. The stainless steel collection vessel was then washed with small
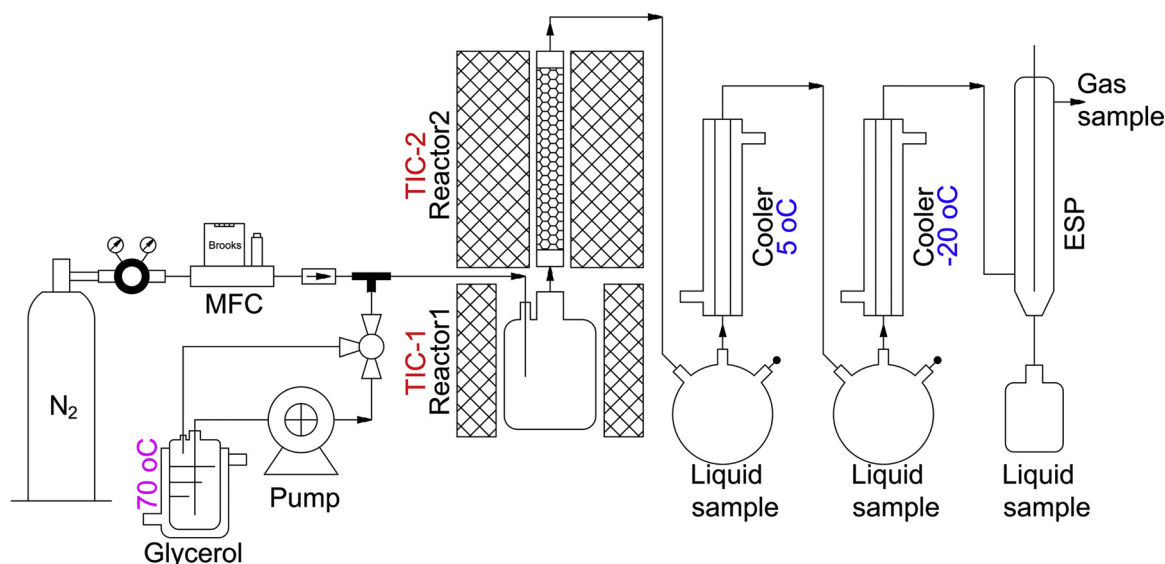
Fig. 1. Schematic representation of the continuous bench scale unit.

amounts of THF to collect all the liquid products. The char formed in the upper bed, coke deposited on the catalysts, liquid (aqueous and oil) products and gas products were analyzed by weighing, elemental (C) analysis and GC–MS to determine the mass and carbon balance during the *ex-situ* catalytic pyrolysis of crude glycerol.

2.3.3. Catalyst deactivation and regeneration in a dedicated bench scale unit (with a continuous crude glycerol feed rate of 200 g h^{-1})

A dedicated bench scale unit was used for the *ex-situ* catalytic pyrolysis of glycerol. Typically, it was possible to convert 5 kg of crude glycerol per day. A schematic representation of the set-up is depicted in Fig. 1. Reactor 1, operated at 520 °C, was continuously fed with crude glycerol (200 g h^{-1}, 70 °C) and purged with a N$_2$ flow (1500 ml min^{-1}, Linde, NL). The vapours were passed to reactor 2, consisting of a packed bed reactor containing 200 g catalysts (1–2 mm average particle size) with a bed height of 15 cm operated at 536 °C. The products of reactor 2 were cooled using a two stage condensation sequence. The first condensor was operated at 5 °C using cooled tap water, the second one was operated at −20 °C using cooled methanol. Finally, the remaining aerosols were collected using an electrostatic precipitator (ESP) operated at 7.5 kV. The liquid products were collected separately and mixed together to be analyzed by GC–MS. The BTX weight yield and carbon yield were calculated by using Eqs. (1) and (2).

$$BTX \ yield \ (wt. \ \%) = \frac{weight \ of \ BTX \ product}{weight \ of \ crude \ glycerol \ feed} \times 100 \qquad (1)$$

$$BTX \ carbon \ yield \ (\%) = \frac{mol \ of \ carbon \ in \ BTX \ product}{mol \ of \ carbon \ in \ the \ crude \ glycerol \ feed} \times 100 \qquad (2)$$

After 4–5 h time on stream (TOS), the BTX yield gradually decreased, indicating some deactivation of the catalysts (termed as Cat-D). The catalyst deactivation percentage (D) was calculated using Eq. (3).

$$D \ (\%) = \frac{initial \ BTX \ yield - final \ BTX \ yield}{initial \ BTX \ yield} \times 100 \qquad (3)$$

To investigate catalyst regenerability and reusability, catalyst recycling experiments were carried out. The deactivated catalysts were regenerated in the reactor under air at 600 °C for 8 h. The obtained catalysts were abbreviated as Cat-Ri, where i indicates the number of regeneration steps the catalyst was subjected to. The turnover number (TON) of the fresh and regenerated catalysts during the investigated TOS was calculated using Eq. (4).

$$TON \left(mol_{BTX} \big/ mol_{acid \ site} \right)$$
$$= \frac{total \ BTX \ production \ during \ investigated \ TOS}{total \ acid \ sites \ according \ to \ Pyrodine-IR \ analysis} \qquad (4)$$

2.4. Catalyst characterization

Nitrogen adsorption-desorption isotherms of the catalysts were obtained at 77 K on an ASAP 2420 Surface Area and Porosity Analyzer (Micromeritics, USA). Catalysts were degassed at 300 °C for 12 h prior to the measurements. The surface area was measured using the *Brunauer-Emmett-Teller* (BET) method in the P/P_o range of 0.05–0.25. Pore size distributions (PSD) were calculated from the desorption branch of the isotherms according to the Barrett-Joyner-Halenda (BJH) method. The total pore volume was estimated by a single point desorption at $P/P_o = 0.98$. The micropore area and volume were calculated using the *t*-plot method.

X-ray diffraction (XRD) spectra of the catalysts were collected on a D8 Advance Powder Diffractometer (Bruker, Germany) with Cu Kα radiation (λ = 1.5418 Å) operated at 40 kV and 40 mA and using a LYNXEYE detector (1D mode) in a 2θ scan range of 5–50°. The relative crystallinity of ZSM-5/bentonite catalysts was calculated according to an ASTM standard [21], which compares the peak height of the 2θ reflection at 24.37° of the catalysts (H$_c$) to that for ZSM-5 (H$_{ZSM-5}$) by using Eq. (5).

$$Relative \ crystallinity \ (\%) = \frac{H_c}{H_{ZSM-5}} \times 100 \qquad (5)$$

The morphology of the catalysts was determined using a Tecnai T20 Transmission Electron Microscope (TEM, FEI, NL) equipped with Gatan 2k × 2k CCD camera at an accelerating voltage of 200 keV. The catalysts were dispersed ultrasonically in ethanol and deposited on a carbon-coated copper grid prior to measurement. Local elemental analysis was performed using a X-Max T80 SDD Energy Dispersive X-ray Detector (EDX, Oxford, UK).

Inductively coupled plasma atomic emission spectroscopy (ICP-AES) was carried out using an Optima 7000 DV Optical Emission Spectrometer (PerkinElmer, USA) to determine the SiO$_2$/Al$_2$O$_3$ mole ratio of the catalysts. Prior to analyses, the catalysts were dissolved in a 3 wt.% HF solution overnight.

Atomic absorption spectrometry (AAS) was performed on an AAnalyst 200 (Perkin Elmer, USA) to determine the Na content of the

catalysts and crude glycerol.

Thermogravimetric analysis (TGA) was carried out on TGA/ SDTA851e Analyzer (Mettler-Toledo, USA). The catalysts were heated in a ceramic crucible from 30 °C to 900 °C at the heating rate of 10 °C min^{-1} under a flow of air of 100 ml min^{-1}. To compensate for matrix effects, TGA's were also perfromed using the ceramic crucibles without catalysts. The TG curves shown in this paper are corrected TGA curves.

Magic angle spinning (MAS) solid state nuclear magnetic resonance (SSNMR) spectra were recorded using a AV-I 750 MHz spectrometer (Bruker, Germany) at 17.6 T, in which ^{27}Al resonates at 195.48 MHz. The catalysts were packed in 4 mm zirconium rotors and analysed at a magic angle spin rate of 54.74.

NH$_3$-TPD measurements were carried out using an AutoChem II system (Micromeritic, USA) equipped with a thermal conductivity detector (TCD). The catalysts were pretreated at 550 °C for 1 h under a He stream (50 ml min^{-1}). After cooling to 100 °C, NH$_3$ in He (1.0 vol.%, 50 ml min^{-1}) was introduced and the sample was kept at these conditions for 1 h. Subsequently, the catalysts were purged with He (50 ml min^{-1}) to remove the weakly adsorbed NH$_3$, followed by heating the samples to 550 °C using a temperature ramp of 10 °C min^{-1}. The desorbed products were detected by TCD which was calibrated for NH$_3$ analysis. The dry weight of the catalysts was re-calculated using the experimentally determined weight loss at 550 °C using TGA.

Pyridine-IR measurements were performed on a Nicolet 6700 FT-IR spectrometer (Thermo Fisher Scientific, USA) using an in house made cell. The cell was connected to a vacuum-adsorption device with the possibility to work at pressures below 10^{-3} Pa. 50 mg of the catalyst was placed in a die and pressed at 3 ton cm^{-2} for 5 s to prepare a pellet with a diameter of 10 mm. The pellet was pre-heated at 350 °C for 4 h under vacuum and subsequently cooled to 25 °C. The pyridine vapor was then introduced, followed by an evacuation step at 300 °C for 30 min an then the sample was cooled to 25 °C. The dry weight of the catalysts was re-calculated using the experimentally determined weight loss at 300 °C using TGA.

Elemental analysis (C and H) of the catalysts were performed using an EuroEA3000 Elemental Analyzer (Eurovector, Italy). The samples were analysed in duplicate and the average value is given.

3. Results and discussions

3.1. Effect of the ZSM-5 to bentonite ratio on BTX yields

The effect of ZSM-5 to bentonite ratio (90/10, 80/20 and 60/40, wt./wt.) in the catalyst on BTX yields were screened in a microgram scale TMR (Section 2.3.1). Pyrolysis of glycerol was performed at 500 °C, the catalytic upgrading of the pyrolysis vapors was carried out at 550 °C. The product distribution based on peak area percentages from GC analyses is shown in Figure S1. Glycerol was completely converted to mainly monocyclic and polycyclic aromatics. Generally, the fraction of non-BTX, GC detectable products were less than 20% (peak areak percentage). Because of the complexity of the products, only the yields of BTX, which are of commercial interest, were determined (Section 2.3.1). The yields as a function of the ZSM-5 to bentonite ratio are shown in Fig. 2. Typically measurements were performed in triplicate and the average BTX yields are given. High BTX yields of *ca.* 15 wt.% (34.6% carbon yield) were obtained over ZSM-5 with a selectivity to benzene of 27%, 45% to toluene and 28% to xylenes. The addition of bentonite had a limited effect on the BTX yields, which was also observed by Dao *et al.* [14] for the catalytic pyrolysis of 55 wt.% glycerol/methanol mixtures using powdered catalysts. However, the selectivities to the individual compounds in the BTX mixture changed significantly and more benzene (40%) was formed at the expense of xylenes when 10 wt.% of bentonite was added to the catalyst formulation. Notably, these selectivities were maintained when the ZSM-5 to bentonite ratio was reduced from 90/10 to 60/40. Catalyst
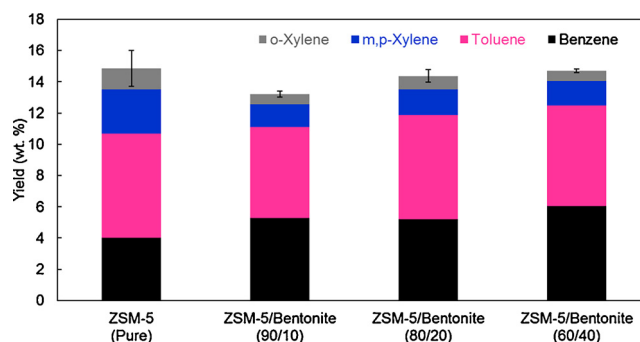

Fig. 2. BTX yields for the catalytic pyrolysis of glycerol over ZSM-5 and ZSM-5/ bentonite catalysts (TMR data).

formulations with a higher bentonite content could not be tested as it proved difficult to prepare such catalysts due to insufficient mechanical strength. Accordingly, it was decided to use the ZSM-5/bentonite (60/ 40) catalysts for subsequent studies.

3.2. Characterization of the ZSM-5/bentonite (60/40) catalysts

The textural properties of the fresh ZSM-5/bentonite (60/40) catalysts (Cat-F) were investigated by N$_2$ physisorption. It showed a combination of type I (in the intial low P/P$_0$ region) and type IV (at higher relative pressure) isotherms according to the IUPAC classification system [22], indicating that the structure contains both micro- and mesopores [23] (Fig. 3A-c). The presence of the latter is also observed
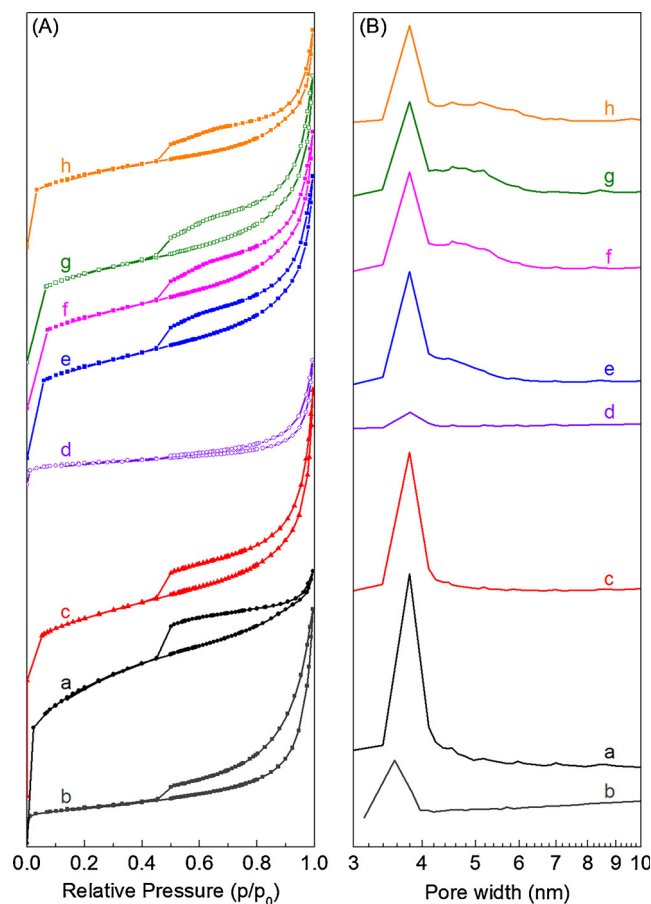

Fig. 3. Nitrogen adsorption/desorption isotherms (A) and pore size distribution (B) of (a) ZSM-5, (b) bentonite, (c) Cat-F, (d) Cat-D, (e) Cat-R1, (f) Cat-R2, (g) Cat-R4 and (h) Cat-R11.

Table 2
Characteristics of ZSM-5, bentonite, and fresh, deactivated and regenerated ZSM-5/bentonite catalysts.

| Sample	S_{BET} (Total) ($m^2 g^{-1}$)[a]	Pore volume (Total) ($cm^3 g^{-1}$)[a]	S_{BET} (Micro) ($m^2 g^{-1}$)[a]	Pore volume (Micro) ($cm^3 g^{-1}$)[a]	Relative crystallinity (%)[b]	Si/Al (mol:mol)[c]	Si/Al (mol:mol)[d]	I_{EFAI}/I_{FAI}[e]	C (wt.%)[f]	H (wt.%)[f]	Na (wt.%)[g]
ZSM-5	369	0.20	270	0.12	100	11.8	9.4	0.1	–	–	0.04
Bentonite	17	0.07	2	0.0007	–	2.4	1.9	–	–	–	1.6
Cat-F	209	0.17	152	0.07	50	5.0	4.4	0.5	0.03	0.5	1.3
Cat-D	30	0.04	16	0.008	60	4.3	4.4	0.5	9.3	0.5	–
Cat-R1	192	0.15	140	0.07	42	4.3	4.3	0.4	–	–	1.2
Cat-R2	183	0.15	131	0.06	43	3.8	4.2	0.4	–	–	1.4
Cat-R4	182	0.15	131	0.06	43	4.7	4.2	0.3	0.03	0.4	–
Cat-R11	158	0.12	113	0.05	31	5.2	4.2	0.04	0.05	0.3	2.2

[a] BET.
[b] XRD.
[c] TEM-EDX.
[d] ICP.
[e] NMR.
[f] EA.
[g] AAS.

visually from the BJH-PSD (Fig. 3B-c), showing a sharp distribution in the mesoporous range (3–4.5 nm), and centered at 3.8 nm. The hysteresis features of Cat-F (Fig. 3A-c) shows a combination of type H2 [22] (corresponding to the cylindrical and slit-like pores of ZSM-5 [23], Fig. 3A-a) and type H3 [22] (related to the plate-like pores of bentonite, Fig. 3A-b). The calculated textural data are presented in Table 2. The specific surface area of Cat-F was 209 $m^2 g^{-1}$, which is slightly smaller than the calculated surface area of 228 $m^2 g^{-1}$ based on the individual weight fraction of ZSM-5 and bentonite in the formulation and the individual surface areas, indicating interactions between the two components. The micropore volume of Cat-F is 0.07 $cm^3 g^{-1}$, which is similar to the individual components, indicating that the micropores are maintained during preparation. Thus, ZSM-5 and bentonite clearly interact in the matrix, though likely only by the external surfaces as the micropore volumes are not affected.

The XRD pattern of ZSM-5 (Fig. 4-a) shows the typical features of a MFI framework type zeolite [24] with high crystallinity. The two peaks (♥) at 2θ = 7.94° and 8.86°, which correspond to the [011] and [200] planes, were used to identify the presence of ZSM-5 [23]. The XRD pattern of bentonite (Fig. 4-b) displayed the structures of montmorillonite (2θ = 19.80° and 35.11°), quartz (2θ = 26.61°) and Na-feldspar (2θ = 27.98°) [25]. As expected, Cat-F shows XRD patterns of both the parent ZSM-5 and bentonite (Fig. 4-c). The relative crystallinity of Cat-F (Table 2) is 50%, which is smaller than based on the weight fraction of ZSM-5 and bentonite (60%) in the formulation, indicating the formation of framework defects during catalyst preparation.

Representative high resolution TEM images of bentonite, ZSM-5 and Cat-F are depicted in Fig. 5. The presence of a highly ordered lattice fringe is observed for ZSM-5 (Fig. 5-a), in line with literature data [26,27]. This indicates that the ZSM-5 is highly crystalline, which is consistent with the XRD results. Cat-F (Fig. 5-c) also exhibited the typical lattice structure of ZSM-5 (Fig. 5-a). The TEM-EDX analysis data are displayed in Figure S2 and the calculated Si/Al mole ratios are tabulated in Table 2. The Si/Al mole ratio of Cat-F was 5.0, which is line with ICP-AES analysis (4.4). However, the value is much lower than calcutated based on the weight fraction of ZSM-5 and bentonite in the catalyst formulation and the Si/Al ratio for the individual components (8.0 for TEM-EDX analysis and 6.4 for ICP-AES analysis). This seems to be an indication for some leaching of Si [28] during catalyst preparation.

The TG curve of ZSM-5 (Fig. 6-a) shows a prominent weight loss peak below 220 °C (6.7 wt.%), which is related to the removal of adsorbed water. No significant weight loss was observed for ZSM-5 when heated above 220 °C, in line with literature data [29]. Two distinct weight loss regions were observed for bentonite (Fig. 6-b), which are
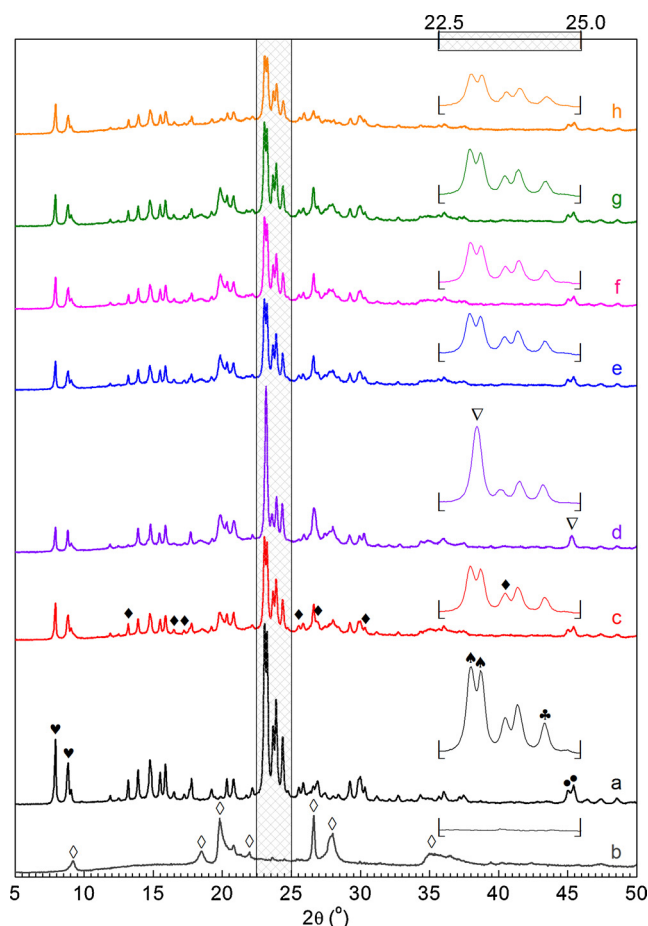
Fig. 4. XRD patterns of (a) ZSM-5, (b) bentonite, (c) Cat-F, (d) Cat-R1, (e) Cat-R1, (f) Cat-R2, (g) Cat-R4 and (h) Cat-R11.

attributed to the desorption of water from the interlamellar region (30–150 °C, 1.1 wt.%) and dehydroxylation (150–750 °C, 4.4 wt.%) [30,31]. The weight loss due to dehydroxylation is comparable with literature data [30,31]. However the interlayer water content is much lower than reported, likely due to the pretreatment of the bentonite at 500 °C in air before use. TGA curves for Cat-F (Fig. 6-c) displayed the combined features of ZSM-5 and bentonite.

The local environments of the Al and Si atoms were further investigated by MAS NMR spectroscopy. The ^{27}Al MAS NMR spectrum of
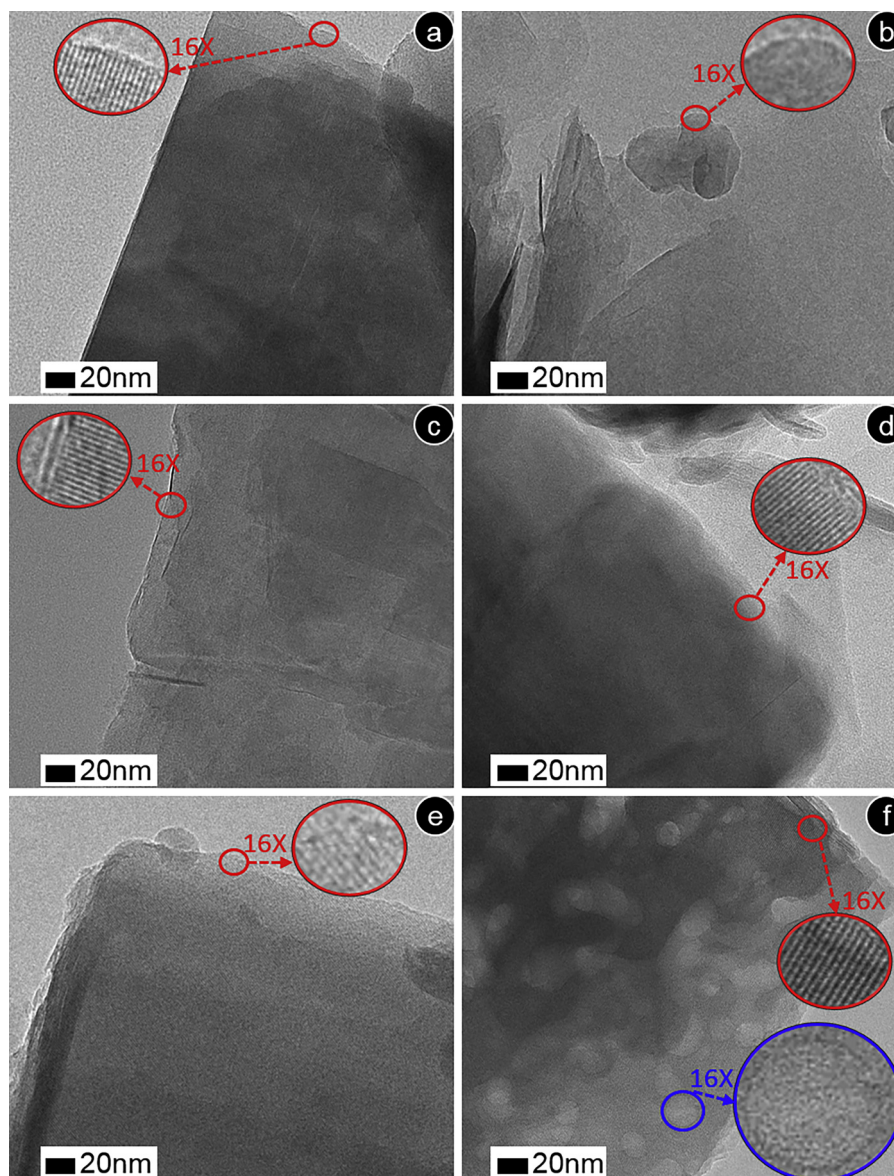
Fig. 5. TEM images of (a) ZSM-5, (b) bentonite, (c) Cat-F, (d) Cat-D, (e) Cat-R1 and (f) Cat-R11.
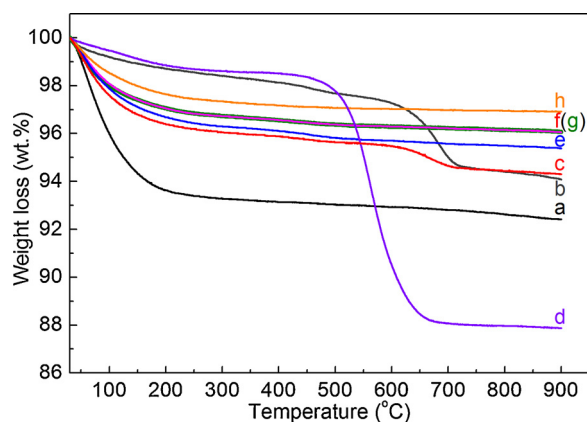

Fig. 6. TG curves of (a) ZSM-5, (b) bentonite, (c) Cat-F, (d) Cat-D, (e) Cat-R1, (f) Cat-R2, (g) Cat-R4 and (h) Cat-R11.

ZSM-5 (Fig. 7A-a) shows two distinct peaks centered at δ = 53.2 ppm and δ = -1.0 ppm, which are assigned to tetrahedrally coordinated Al in the zeolite framework (FAl) and octahedrally coordinated extra framework Al (EFAl) [29], respectively. Two peaks centered at δ = 61.7 ppm (overlapped by the spinning sideband at δ = 70.0 ppm) and δ = 4.0 ppm are observed, indicating the existence of both Al in tetrahedral and octahedral sites [32]. Accordingly, Cat-F (Fig. 7A-c) also exhibts tetrahedrally (δ = 54.7 ppm) and octahedrally (δ = 3.4 ppm) coordinated Al species. The calculated EFAl/FAl peak intensity ratio is listed in Table 2 and shows that Cat-F has a higher I_{EFAl}/I_{FAl} value than ZSM-5 due to the contribution of bentonite.

The ^{29}Si MAS NMR spectrum of ZSM-5 (Fig. 7B-a) shows a broad peak at δ = -112.5 ppm with a shoulder at δ = −106.0 ppm, corresponding to the various Q^4 linkages in the framework (Q^4(4Si, 0Al), Q^4(3Si, 1Al) and Q^4(2Si, 2Al)) [33,34]. The ^{29}Si MAS NMR spectrum of bentonite (Fig. 7B-b) displays resonances at δ = −93.9 ppm and δ = −107.7 ppm, which were assigned to Q^3(3Si, 0Al) in the chain branching sites [35] and α-quartz [36], respectively. The former peak is typically for montmorillonite [36,37]. However, comparatively, the peak is broadened due to the partial loss of interlayer water and dehydroxylation [37] by the pretreatment at 500 °C, in line with the TG
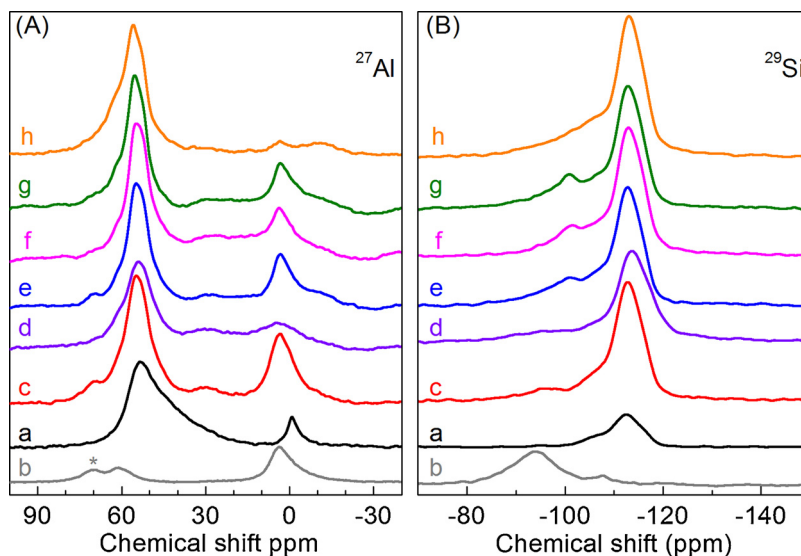
Fig. 7. ^{27}Al (A) and ^{29}Si (B) MAS NMR spectra of (a) ZSM-5, (b) bentonite, (c) Cat-F, (d) Cat-D, (e) Cat-R1, (f) Cat-R2, (g) Cat-R4 and (h) Cat-R11.

analysis results. The presence of the quartz structure is also supported by the XRD data (Fig. 4-b).

As expected, the ^{29}Si MAS NMR spectrum of Cat-F (Fig. 7B-c) shows the peaks observed for the individual components. Notably, the Q^3(3Si, 0Al) resonance in bentonite is shifted from $\delta = -93.9$ to $\delta = -95.6$ ppm, an indicaton for further dehydration of interlamellar water in bentonite [37] during catalyst preparation.

The NH$_3$-TPD curve of ZSM-5 (Fig. 8-a) shows two distinct peaks centered at 200 °C and 360 °C, which are typical for ZSM-5 zeolites [23,38] and correspond to the weak and strong acidic sites, respectively. Quantification of the total acidiy is provided in Table 3. Comparatively, the acidity of bentonite is very low (Fig. 8-b). Cat-F (Fig. 8-c) exhibits one prominent peak related to the weak acid sites, which originates from the ZSM-5 catalyst, implying that most of the strong acidic sites of ZSM-5 are lost during catalyst preparation. Typically, these strong acidic sites in ZSM-5 are attributed to Brönsted acidic sites [39,40].
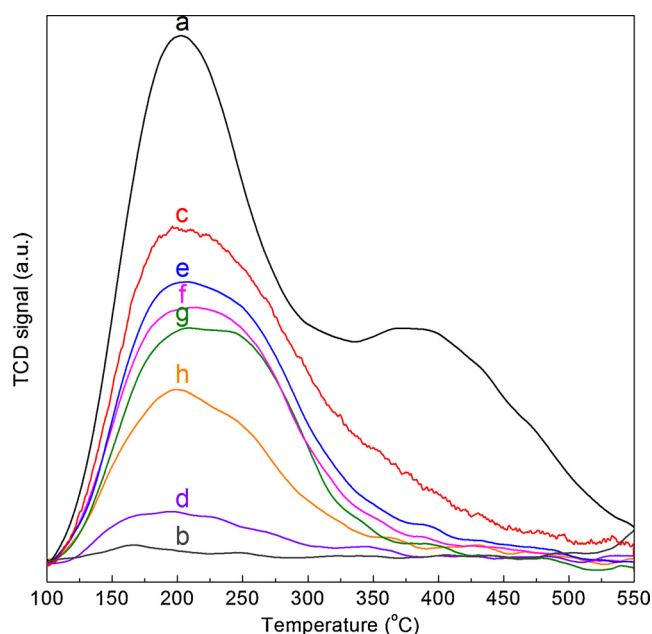
Table 3
Acidity properties of ZSM-5, bentonite, and fresh, deactivated and regenerated ZSM-5/bentonite catalysts.

Sample	Total (μmol NH$_3$ g^{-1} sample)[a]	L-Py (1455)	B-Py (1545)	Total (B + L)	B/L[b]
		(μmol Pyridine g^{-1} sample)[b]			
ZSM-5	946	58.1	77.4	135.5	1.3
Bentonite	–	–	–	–	–
Cat-F	542	31.0	14.6	45.6	0.5
Cat-D	69	4.2	0.3	4.4	0.1
Cat-R1	409	8.5	4.1	12.6	0.5
Cat-R2	353	6.3	2.9	9.1	0.5
Cat-R4	328	5.7	2.7	8.4	0.5
Cat-R11	221	3.9	0.9	4.8	0.2

[a] NH$_3$-TPD.
[b] Pyridine-IR.

Fig. 8. NH$_3$-TPD profiles of (a) ZSM-5, (b) bentonite, (c) Cat-F, (d) Cat-D, (e) Cat-R1, (f) Cat-R2, (g) Cat-R4 and (h) Cat-R11.
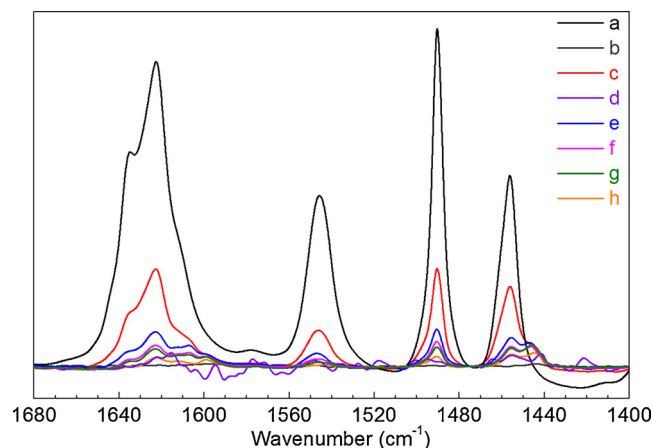

Fig. 9. Pyridine-IR spectra of (a) ZSM-5, (b) bentonite, (c) Cat-F, (d) Cat-D, (e) Cat-R1, (f) Cat-R2, (g) Cat-R4 and (h) Cat-R11.

To gain more insights in the decrease of Brönsted acid sites of the catalysts during catalyst preparation, pyridine-IR measurements were performed. The pyridine-IR spectrum of ZSM-5 (Fig. 9-a) displays a broad peak between 1590–1660 cm^{-1} and three individual bands at 1545 cm^{-1}, 1490 cm^{-1} and 1455 cm^{-1}. These correspond to the C-CN vibrations of protonated pyridine (BPy), H-bonded pyridine (HPy) and
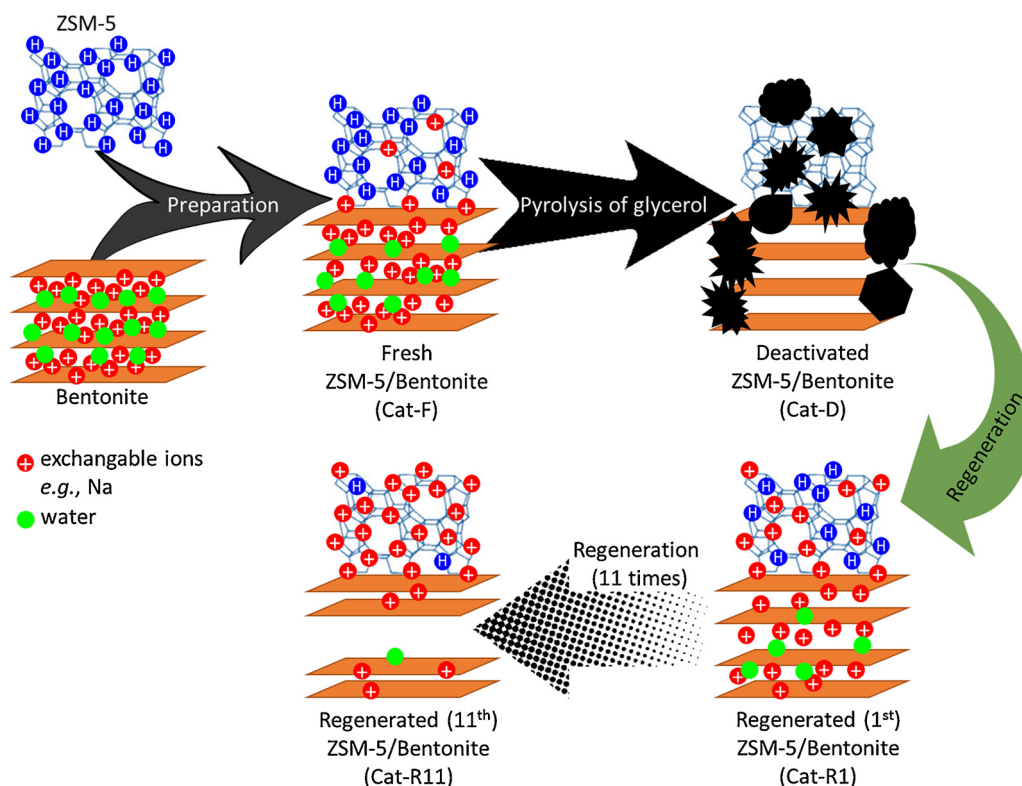
Scheme 1. Overview of changes in the ZSM-5/bentonite catalyst structure during preparation, deactivation and regeneration showing reversible and irreversible decativation mechanisms.

unsaturated metal coordinated pyridine (LPy), respectively [41]. The formation of B-Py (1545 cm^{-1}) and L-Py (1455 cm^{-1}) species indicates the presence of Brönsted and Lewis acidic sites in ZSM-5 [40,42]. Cat-F, prepared from ZSM-5 and the non-acidic bentonite (Fig. 9-b) shows a low acidity (Fig. 9-c, Table 3). The Lewis acidity of Cat-F is 53% of that of ZSM-5, which is slightly lower than expected on the weight fraction (60%) of ZSM-5 in Cat-F. This indicates that the amount of Lewis acid sites in ZSM-5 are slightly decreased during preparation of the ZSM-5/bentonite catalysts. In contrast, the Brönsted acidity of Cat-F is only 19% of that of ZSM-5, in line with the NH$_3$-TPD results discussed above. TEM-EDX images (Figure S2-c) show that many ZSM-5 particles in Cat-F contain Na and Fe. Simultaneously, the amount of Na in the bentonite particles is reduced, indicating some migration of Na cations from bentonite to ZSM-5. This is expected to result in a decrease in the number of Brönsted acid sites, in line with the pyridine-IR and NH$_3$-TPD data.

Based on the extensive catalyst characterisation studies discussed above, it is clear that the structure of Cat-F is not simply a physical mixture of bentonite and ZSM-5. For instance, cations (*e.g.*, Na and Fe) of bentonite exchange with the protons of ZSM-5 resulting in a decrease of the Brönsted acid sites of ZSM-5 (Scheme 1). In addition, there appears to be an interaction between the bentonite and ZSM-5 particles, as evident from the changes in the external surface in Cat-F compared to the individual components. However, Bentonite does not fill the internal micropores of ZSM-5. The amount of interlamellar water present in the parent bentonite was slightly reduced during catalyst preparation (Scheme 1).

3.3. Ex-situ catalytic pyrolysis of crude glycerol over ZSM-5/bentonite (60/40) catalysts in a batch gram scale unit

The *ex-situ* catalytic pyrolysis of crude glycerol (1 g) over the above ZSM-5/bentonite (60/40, Cat-F, 3 g) was tested in a batch gram scale reactor (Section 2.3.2) to determine the mass and carbon balance
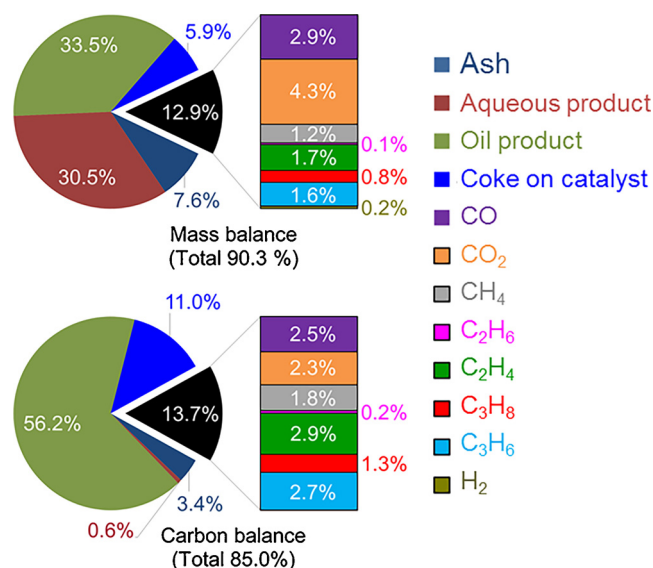
Fig. 10. Mass and carbon balance of *ex-situ* catalytic pyrolysis of crude glycerol over ZSM-5/bentonite catalyst (Cat-F) in the batch gram scale unit.

closure. A very satisfactorily total mass balance closure (90.3%, Fig. 10) was obtained, showing 64.0 wt.% of liquids (aqueous and oil phases), 13.5 wt.% of solids (char and coke) and 12.9 wt.% of gas products were formed.

Determination of the carbon content of the solid and liquid phases allowed calculation of the carbon balances. 8.9% of the carbon in the crude glycerol was converted to gaseous hydrocarbons (C$_1$-C$_3$ alkanes and alkenes). A small fraction of carbon was transformed into CO (2.5%) and CO$_2$ (2.3%) indicating that the conversion of glycerol to hydrocarbons over ZSM-5/bentonite catalysts *via* deoxygenation mostly
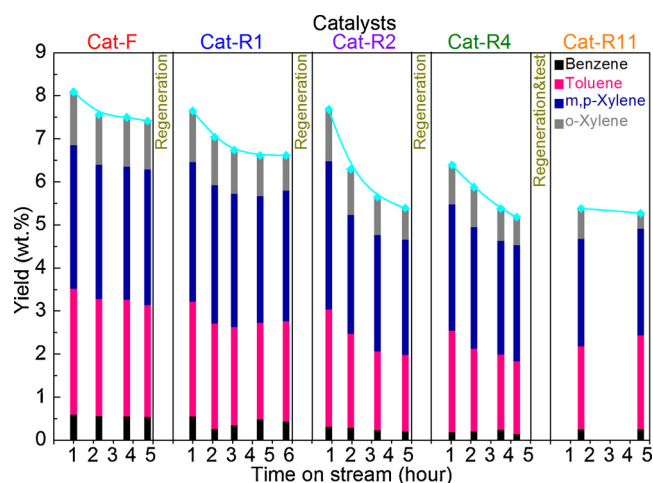
Fig. 11. BTX yield of catalytic pyrolysis of crude glycerol over fresh and regenerated ZSM-5/bentonite catalysts in the bench scale unit.

Fig. 12. TG-DTG curves of Cat-D.

follows dehydration (-H$_2$O, *ca.* 85%). The low extent of decarboxylation (-CO$_2$, *ca.* 10%) and decarbonylation (-CO, *ca.* 5%) well explains the high carbon yield (56.2%) for the liquid oil products (monocyclic and polycyclic aromatics). However, about 11% of the carbon in the crude glycerol was transformed into coke and deposited on the catalysts, an aspect which will be further elaborated in the following section.

GC–MS analysis of the oil fraction shows BTX yields of *ca.* 15.5 wt.% (36.2% carbon yield), in good agreement with BTX yields of *ca.* 14.7 wt. % (34.4% carbon yield) over the ZSM-5/bentonite (60/40) catalysts observed in the small scale TMR unit (Section 3.1 and Fig. 2).

3.4. Catalytic pyrolysis of crude glycerol over ZSM-5/bentonite (60/40) catalysts in a bench scale unit

Cat-F (200 g) was further tested in the continuous bench scale unit (Section 2.3.3, Fig. 1) to evaluate its performance for the catalytic pyrolysis of crude glycerol (200 g h^{-1}). The product distribution based on peak area percentages is shown in Figure S3. The crude glycerol was completely converted in all the experiments. A BTX yield of 8.1 wt.% (14.6% carbon yield) was obtained over Cat-F during a time on stream (TOS) of 1.0 h (Fig. 11). This value is much lower than the yield (*ca.* 15 wt.%, Fig. 2) obtained over the same catalyst in the batch mg scale TMR reactor (Section 3.1) and gram scale unit (Section 3.3). This observation may be rationalised by considering that the heating rate of glycerol in both set-ups differs considerably. The heating rate in the TMR (*ca.* 200–300 °C s^{-1}) is by far higher than that in the continuous bench scale unit. This is of high relevance as it has been reported that lower heating rates for the thermal pyrolysis of glycerol leads to higher amounts of char [6]. Furthermore, the slight difference in the operation temperature in the TMR and the bench scale unit is expected to affect the BTX yield to some extent. In addition, the products of the bench scale unit are condensed before analysis, in contrast to the experiments in the TMR device. As such, incomplete condensation may result in some loss of volatile products (particularly benzene).

Some deactivation (D = 6.6%) of the catalysts was observed for the first 2.3 h on stream (Fig. 11). Upon longer times on stream (TOS), the rate of deactivation is reduced (D = 7.4% and 8.4% at TOS of 3.7 h and 4.7 h, respectively). These findings are in line with literature data for the *ex-situ* pyrolysis of glycerol using powdered ZSM-5 catalysts (sub-mm particle sizes) [11,18,43]. The product distribution (Figure S3) shows the presence of phenol (and substituted phenols) and n-alkanes (C$_7$−C$_{11}$) after a TOS of 3.7 h, indicating that the rates for deoxygenation and aromatization are slightly reduced by partial deactivation of active sites and thus the selectivity of the catalytic process changes accordingly. The calculated TON of Cat-F during TOS of 4.7 h is
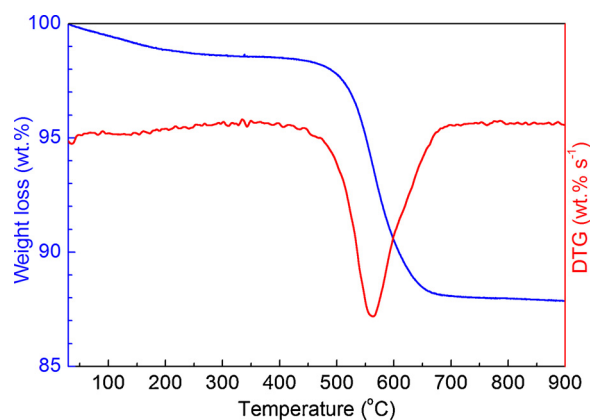
8 mol$_{total\ BTX}$/mol$_{acid\ sites}$, indicating that Cat-F acts as a true catalyst and not as a stoichiometric agent.

The deactivated ZSM-5/bentonite (60/40) catalysts after 4.7 h on stream (termed as Cat-D) was characterized in detail to determine possible deactivation pathways. TG analysis (Fig. 12) for Cat-D shows a considerable weight loss in the temperature range of 450–650 °C, indicating the presence of *ca.* 10.5 wt.% of coke on the catalysts (Scheme 1) [10,11]. These findings are supported by elemental analysis (Table 2), showing the presence of 9.3 wt.% of carbon on the catalysts. The DTG curve shows a large endothermic peak at T$_m$ of 562 °C, indicating the presence of a hard coke. This is supported by the elemental analysis which shows a low H/C ratio (< 0.5, Table 2), typical for a hard coke. Coke deposition results in a considerable reduction in the specific surface area and total pore volume of Cat-D (Table 2) compared to Cat-F. The XRD pattern of Cat-D (Fig. 4-d) shows that the peaks (♦) at 2θ = 13.19°, 16.50°, 17.23°, 23.67°, 25.52°, 26.89° and 30.32°, assigned to [002], [-212], [-231], [-511], [-233], [600] and [503] planes of the ZSM-5 particles in Cat-F, respectively, are severely reduced or even disappeared. Simultaneously, two new peaks (∇) at 2θ = 23.17 and 45.29 are formed, though these overlapp with peaks (▲) at 2θ = 23.07° and 23.23° (assigned to [051] and [−501] of planes of ZSM-5) and the peaks (●) at 2θ = 45.02° and 45.43° (assigned to [0100] and [1000] of planes of ZSM-5). Because, these two new peaks (∇) disappear (Fig. 4-e) after regeneration of the catalyst by an oxidative treatment, they likely arise from the formation of coke with a high crystallinity. XRD results indicate that the coke is mainly deposited on ZSM-5 and not on the bentonite. This is also confirmed by the N$_2$ adsorption/desorption isotherms of Cat-D (Fig. 3-d), where the typical H2 type hysteresis loop from ZSM-5 almost completely disappeared.

Coke deposition also affects the total acidity of the catalysts. For instance, the total acidity of Cat-D (Table 3) as measured by NH$_3$-TPD is only 13% of that of the fresh catalysts (Cat-F). These findings are supported by pyridine-IR results (Fig. 9 and Table 3). Of interest is the observation that particularly the strong acid sites are absent in the spent catalysts (Cat-D, Fig. 8-d). This suggests that the strong acidic sites of Cat-F are covered by coke. Again, these findings are also supported by the pyridine-IR results (Table 3), showing that only 2% of the original Brönsted acid sites are retained. Comparatively, a higher fraction of Lewis acid sites (*ca.* 14%) were retained on Cat-D, indicating that the Brönsted acid sites are deactivated much faster than the Lewis acid sites during the catalytic pyrolysis of glycerol.

Thus we can conclude that coke deposition is occurring to a significant extent during reaction and that this leads to a large reduction in acidity (especially Brönsted acidity). Based on the observation of an ordered lattice fringe for Cat-D in TEM images (Fig. 5-d) and the I$_{EFAl}$/I$_{FAl}$ values listed in Table 2, it can be concluded that the lattice structure and framework of the catalysts are not significantly affected.

3.5. Regeneration of the deactivated ZSM-5/bentonite (60/40) catalysts

Cat-D was subjected to an oxidative treatment at 600 °C (Section 2.3.3) to remove the coke deposited on the catalysts. This temperature is based on TG-DTG measurements for Cat-D showing that a high coke combustion temperature (> 562 °C) is required to remove coke. The TG curve of the oxidatively regenerated catalysts (Cat-R1, Fig. 6-e) shows no obvious weight loss in the temperature range of 450–650 °C indicating quantitative coke removal. This is also confirmed by the disappearence of the two peaks (∇, related to coke) in the XRD pattern of Cat-R1 (Fig. 4-e). After regeneration, the textural properties (surface area and pore volume, Table 2) of Cat-R1 are almost similar to the fresh catalysts (Cat-F). For instance, the XRD pattern of Cat-R1 (Fig. 4-e) shows that the peaks (♠ and ●, corresponding to ZSM-5), which were reduced considerably in the spent catalysts (Cat-D, Fig. 4-d), were recovered after regeneration. In addition, a TEM image of Cat-R1 also shows the well orderd lattice structure of the fresh catalysts. However, the relative crystallinity of the regenerated catalysts (42%) was lower than for the fresh catalysts (50%).

The acidity of the regenerated catalysts (Cat-R1) is by far lower than the fresh catalysts (Table 3). A possible explanation for the incomplete recovery of acidity upon regeneration is the possible exchange of basic cations (*e.g.*, Na and Mg) from the bentonite with protons from ZSM-5 during regeneration at elevated temperatures (Scheme 1). This was confirmed by EDX analysis of Cat-R1 (Figure S2-e), showing bentonite particles with lower amounts Na than the fresh ones. Other explanations are sintering of ZSM-5 particles and a collapse of the layered structure of bentonite. The latter was evidenced by the observation of newly formed interparticle pores with a PSD centered at around 4.6 nm on Cat-R1 (Fig. 3B-e). Possibly, further dehydration of the interlamellar structure of bentonite occurs (Scheme 1), which is supported by ^{29}Si NMR analysis (Fig. 7B-e), showing that the resonance assigned to Q3 (3Si, 0Al) is shifted from δ = -95.6 ppm in Cat-F to δ = −101.6 ppm in Cat-R1 [37].

The activity of the regenerated Cat-R1 was tested in the bench scale unit and a BTX yield of 7.7 wt.% (13.8% carbon yield) was obtained (Fig. 11). This value is slightly lower than that for the fresh catalysts (8.5 wt.% BTX), indicating that some irreversible deactivation occurred. Indicative for deactivation is the formation of phenol (and the substituted phenols) and *n*-alkanes (C_7-C_{11}) over Cat-R1 at a TOS of 1.0 h (Figure S3). This lower BTX yield is in line with the lower amounts of acid sites on Cat-R1 compared to the fresh catalysts [9,10,15]. The extent of deactivation of Cat-R1 for the first 2.1 h on stream (D = 8.0%) was higher than for Cat-F (D = 6.6%), which might be due to the lower coke accomodation ability [44] for Cat-R1. It can be seen that the pore volume of Cat-R1 (0.15 cm^3 g^{-1}, Table 2) is sightly reduced as compared to Cat-F (0.17 cm^3 g^{-1}, Table 2) upon regeneration, resulting in less coke migration from micropores to mesopores and thus faster deactivation. These findings are in line by studies reported by Wang *et al.* [10] on the reusability of Sn/ZSM-5 catalysts (sub mm level) for the catalytic pyrolysis of 40% glycerol/methanol mixtures.

3.6. Recycling of regenerated ZSM-5/bentonite (60/40) catalysts

As reported above, catalyst performance of bentonite-ZSM-5 catalysts for the *ex-situ* catalytic fast pyrolysis of glycerol is a function of the TOS and both reversible and irreversible deactivation were observed after 1 recycle/regeneration step. To further determine the extent of irreversible deactivation, 11 reaction-oxidative regeneration cycles were performed and the results are given in Fig. 11. It is evident that the BTX yield gradually decreases with the number of regeneration steps from 7.7 wt.% (13.8% carbon yield) over Cat-R1 to 5.4 wt.% (9.7% carbon yield) over Cat-R11. Furthermore, higher amounts of phenol (and substituted phenols) and *n*-alkanes (C_7-C_{11}) were observed over Cat-R4 at a TOS of 1.1 h and Cat-R11 at a TOS of 1.6 h (Figure S3), indicating that the deoxygenation and aromatization capability of the

catalysts decreased and can only be partially regenerated (irreversible deactivation). The textural properties of the regenerated catalysts (Table 2) were determined and reveal that the surface area and pore volume decrease gradually after 11 regeneration-reaction cycles (Cat-R11). TGA of the regenerated catalysts (Fig. 6) only show a weight loss peak in the range 30–300 °C, associated with the dehydration of interlamellar water in bentonite and adsorbed water on ZSM-5. No obvious weight loss at higher temperatures for the dehydroxylation of bentonite was observed for Cat-R11 (in contrast to Cat-F, Fig. 6) indicating that dehydroxylation is irreversible. Dehydration and dehydroxylation of the bentonite structure result in destruction of its layered structure, giving rise to more and larger interparticle pores in the regenerated catalysts (Scheme 1). This is also evident from the PSD of the regenerated catalysts (Figure 3B), showing that the PSD of the newly formed interparticle pores are wider and shifted from 4.6 nm (Cat-R1) to 5.2 nm (Cat-R11). Changes in the bentonite structure are also evident from the XRD patterns of Cat-R11 (Fig. 4-h) where the peaks (◊) corresponding to bentonite disappeared after 11 regeneration steps. This collapse of the bentonite structure also affects the crystal structure of ZSM-5 and for instance the relative crystallinity of Cat-R11 was considerably lower than for the fresh catalyst (Table 2). This is also reflected in the HR-TEM images of Cat-R11 (Fig. 5-f), which shows inhomogeneities in the lattice fringe of ZSM-5. ICP-AES analysis (Table 2) of the regenerated catalysts shows almost no losses of Si and Al from the catalysts during regeneration. However, the I_{EFAl}/I_{FAl} values, as calculated from ^{27}Al MAS NMR measurements, show a severe decrease in the amount of EFAl when comparing the fresh catalyst with Cat-R11 (Table 2), resulting in a sharp decrease in the Lewis acidity. This was confirmed by pyridine-IR analysis (Fig. 9 and Table 3) showing that the amount of Lewis acid sites was reduced with 87% compared to Cat-F. Moreover, the amount of Brönsted acid sites were also by far lower than for the fresh catalyst and only 6% of the Brönsted acid sites of Cat-F were retained on Cat-R11. This severe decrease in the number of Brönsted acid sites is likely due to ion-exchange of the basic ions from bentonite and possibly also from the crude glycerol with the protons of ZSM-5 during the reaction-regeneration steps (Scheme 1). This is evidenced by the EDX analysis of the regenerated catalysts shown in Figure S2 and the Na content of the catalysts shown in Table 2. NH$_3$-TPD analysis of the regenerated catalysts (Fig. 8 and Table 3) also confirms the reduction of the total acidity. All these above observations (*e.g.*, lowering of the surface area, pore volume, reduced Brönsted and Lewis acidity) likely contribute to the irreversible deactivation of the catalyst after multiple catalyst regeneration steps. However, the calculated TON of Cat-R11 during a TOS of 4.5 h is 41 mol$_{total BTX}$/mol$_{acid sites}$, which is higher than that for Cat-F. This is mainly due to more and excess acidic sites on Cat-F.

4. Conclusions

We have investigated the *ex-situ* catalytic pyrolysis of crude glycerol for the production of bio-BTX using ZSM-5/bentonite catalyst formulations (1–2 mm particle size) in a bench scale unit (200 g catalysts loading). Catalyst performance was studied in detail and it was shown that both reversible and irreversible catalyst deactivation occur. Coke formation on the catalysts was shown to lead to catalyst deactivation, though activity can be regained by using an oxidative regeneration step at 600 °C to remove the coke. However, after one regeneration only 95% of the initial activity was regained, indicating also some irreversible catalyst deactivation. The latter was shown to be due to *i)* collapse of the bentonite structure by removal of interlammellar water and dehydroxylation and *ii)* a reduction in the acidity of the catalysts. The latter is likely due to exchange of cations (*e.g.*, Na) from both the bentonite and the crude glycerol with the protons of ZSM-5.

Acknowledgments

Appendix A. Supplementary data

Supplementary material related to this article can be found, in the online version, at doi:https://doi.org/10.1016/j.apcatb.2018.04.047.

References

[1] M. Ayoub, A.Z. Abdullah, Renew. Sustain. Energy Rev. 16 (2012) 2671–2686.

[2] R. Ciriminna, C. Della Pina, M. Rossi, M. Pagliaro, Eur. J. Lipid Sci. Technol. 116 (2014) 1432–1439.

[3] S. Bagheri, N.M. Julkapli, W.A. Yehye, Renew. Sustain. Energy Rev. 41 (2015) 113–127.

[4] C.H.C. Zhou, J.N. Beltramini, Y.X. Fan, G.Q.M. Lu, Chem. Soc. Rev. 37 (2008) 527–549.

[5] B.L. Dou, V. Dupont, P.T. Williams, H.S. Chen, Y.L. Ding, Bioresour. Technol. 100 (2009) 2613–2620.

[6] F. Fantozzi, A. Frassoldati, P. Bartocci, G. Cinti, F. Quagliarini, G. Bidini, E.M. Ranzi, Appl. Energy 184 (2016) 68–76.

[7] Y.S. Stein, M.J. Antal, M. Jones, J. Anal. Appl. Pyrolysis 4 (1983) 283–296.

[8] E.B. Hemings, C. Cavallotti, A. Cuoci, T. Faravelli, E. Ranzi, Combust. Sci. Technol. 184 (2012) 1164–1178.

[9] S. Tamiyakul, W. Ubolcharoen, D.N. Tungasmita, S. Jongpatiwut, Catal. Today 256 (2015) 325–335.

[10] F. Wang, W.Y. Xiao, L.J. Gao, G.M. Xiao, Rsc Adv. 6 (2016) 42984–42993.

[11] T.Q. Hoang, X.L. Zhu, T. Danuthai, L.L. Lobban, D.E. Resasco, R.G. Mallinson, Energy Fuels 24 (2010) 3804–3809.

[12] Y.-W. Suh, H.-S. Jang, K.-B. Bae, Method for Producing Bio-Aromatics from Glycerol, U.S. Pat. Appl. Publ, Industry-University cooperation Foundation Hanyang Universituy, Seoul, Korea, United States, 2015 p. 11.

[13] Y. Xiao, A. Varma, ACS Energy Lett. 1 (2016) 963–968.

[14] L.H. Dao, M. Haniff, A. Houle, D. Lamothe, Acs Symp. Ser. 376 (1988) 328–341.

[15] W.Y. Xiao, F. Wang, G.M. Xiao, Rsc Adv. 5 (2015) 63697–63704.

[16] A. Shahnazari, Catalytic Co-Conversion of Glycerol and Proton-Donor Species to Gasoline-Range Aromatics Over Alumina, The University of New Brunswick, 2016 p. 113.

[17] R. Le Van Mao, H. Yan, A. Muntasar, N. Al-Yassir, S.L. Suib (Eds.), New and Future Developments in Catalysis, Elsevier, Amsterdam, 2013, pp. 143–173.

[18] G.Q. Luo, A.G. McDonald, Energy Fuels 28 (2014) 600–606.

[19] Y.-W. Suh, M. Shin, Method for Producing Bio-Aromatics from Glycerol, Industry-University Cooperation Foundation Hanyang University, Seoul, Korea, 2016 p. 17.

[20] H.S. Jang, K. Bae, M. Shin, S.M. Kim, C.U. Kim, Y.W. Suh, Fuel 134 (2014) 439–447.

[21] ASTM, ASTM D5758-01: Standard Test Method for Determination of Relative Crystallinity of Zeolite ZSM-5 by X-Ray Diffraction, ASTM International, West Conshohocken, PA, 2011 19428-2959, United States.

[22] K.S.W. Sing, D.H. Everett, R.A.W. Haul, L. Moscou, R.A. Pierotti, J. Rouquerol, T. Siemieniewska, Pure Appl. Chem. 57 (1985) 603–619.

[23] A.S. Al-Dughaither, H. de Lasa, Ind. Eng. Chem. Res. 53 (2014) 15303–15316.

[24] M.M.J. Treacy, J.B. Higgins, Collection of Simulated XRD Powder Patterns for Zeolites, fifth edition, Elsevier Science B.V., Amsterdam, 2007, pp. 278–279.

[25] R. Ruiz, C. Blanco, C. Pesquera, F. Gonzalez, I. Benito, J.L. Lopez, Appl. Clay Sci. 12 (1997) 73–83.

[26] T. Behrsing, H. Jaeger, J.V. Sanders, Appl. Catal. 54 (1989) 289–302.

[27] D. Van Vu, M. Miyamoto, N. Nishiyama, S. Ichikawa, Y. Egashira, K. Ueyama, Microporous Mesoporous Mater. 115 (2008) 106–112.

[28] A.K. Jamil, O. Muraza, R. Osuga, E.N. Shafei, K.H. Choi, Z.H. Yamani, A. Somali, T. Yokoi, J. Phys. Chem. C 120 (2016) 22918–22926.

[29] K. Ramesh, C. Jie, Y.F. Han, A. Borgna, Ind. Eng. Chem. Res. 49 (2010) 4080–4090.

[30] Y.M. Zhang, Q.F. Liu, Z.G. Wu, Y.F. Zhang, J. Therm. Anal. Calorim. 121 (2015) 1287–1295.

[31] L. Andrini, R.M. Toja, M.R. Gauna, M.S. Conconi, F.G. Requejo, N.M. Rendtorff, Appl. Clay Sci. 137 (2017) 233–240.

[32] D. Haffad, A. Chambellan, J.C. Lavalley, Catal. Lett. 54 (1998) 227–233.

[33] K.S. Triantafyllidis, A.G. Vlessidis, L. Nalbandian, N.P. Evmiridis, Microporous Mesoporous Mater. 47 (2001) 369–388.

[34] Z.W. Yu, S.H. Li, Q. Wang, A.M. Zheng, X. Jun, L. Chen, F. Deng, J. Phys. Chem. C 115 (2011) 22320–22327.

[35] E. Lippmaa, M. Magi, A. Samoson, G. Engelhardt, A.R. Grimmer, J. Am. Chem. Soc. 102 (1980) 4889–4893.

[36] J.G. Thompson, Clay Min. 19 (1984) 229–236.

[37] I.W.M. Brown, K.J.D. Mackenzie, R.H. Meinhold, J. Mater. Sci. 22 (1987) 3265–3275.

[38] L. Rodriguez-Gonzalez, F. Hermes, M. Bertmer, E. Rodriguez-Castellon, A. Jimenez-Lopez, U. Simon, Appl. Catal. A-Gen. 328 (2007) 174–182.

[39] K. Na, S. Alayoglu, R. Ye, G.A. Somorjai, J. Am. Chem. Soc. 136 (2014) 17207–17212.

[40] Y. Lou, J. Ma, W.D. Hu, Q.G. Dai, L. Wang, W.C. Zhan, Y.L. Guo, X.M. Cao, Y. Guo, P. Hu, G.Z. Lu, Acs Catalysis 6 (2016) 8127–8139.

[41] M.I. Zaki, M.A. Hasan, F.A. Al-Sagheer, L. Pasupulety, Colloid Surf. A 190 (2001) 261–274.

[42] A. Martin, U. Wolf, S. Nowak, B. Lucke, Zeolites 11 (1991) 85–92.

[43] H.Y. Zhang, Y.T. Cheng, T.P. Vispute, R. Xiao, G.W. Huber, Energy Environ. Sci. 4 (2011) 2297–2307.

[44] S. Hu, Q. Zhang, Y.J. Gong, Y. Zhang, Z.J. Wu, T. Dou, Acta Phys.-Chim. Sin. 32 (2016) 1785–1794.